



Aeroacoustics and Artificial Neural Network Modeling of Airborne Acoustic Emissions During High Kinetic Energy Thermal Spraying

Spyros Kamnis¹ · Konstantina Malamoussi² · Alex Marrs³ · Bryan Allcock⁴ · Konstantinos Delibasis²

Submitted: 14 April 2019 / in revised form: 13 May 2019 / Published online: 24 May 2019
© ASM International 2019

Abstract This work describes an online, non-destructive monitoring technology for thermal spray coating processes based on the airborne acoustic emissions (AAE) in the booth. First, numerical simulations were carried out to probe into the relationship between AAE signals and the frequency spectrum generated during high velocity-oxy-fuel thermal spray. The experimental part consisted of spraying a plane substrate. The torch was traversed in front of the substrate at a constant speed, 90° impact angle and for different combinations of standoff distance and powder feed rate. The AAE signals were acquired using a broadband piezoelectric sensor positioned at a fixed point near the torch, and the experimental power spectrum of the signal was processed and compared with model predictions. A neural network-based model was implemented capturing and representing the complex relationships between the power spectrum of the AAE and the resulting coating microhardness. The research outcomes demonstrate that the sound contains detectable information associated with spray parameters such as powder feed rate, spray distance and the resulting coating microhardness. The proposed technology can be used to detect process flaws so that deviations from the optimum spraying conditions can be detected and corrected promptly.

Keywords acoustic emissions · artificial neural networks · computational fluid dynamics · HVOF · in situ monitoring · process diagnostics · thermal spray

Introduction

Advanced control systems, based on programmable logic controllers, digital mass flow meters and controllers, as those used in thermal spraying equipment lead to reproducible primary input parameters (gas flow rates, pressures, feed rates, gun movement), but they are not technically capable of monitoring the variation of the coating quality resulting from permanent or sudden modifications and fluctuations in the system hardware. Nozzle wear, clogging, troubling in feeding lines, gas leaks, tube erosion, etc., are not detectable by these systems but are extremely important for practical applications.

Deviation from the optimal spraying parameters can produce substantial variation in the quality of the applied coating microstructure. These quality-related issues can result in catastrophic failures or even life-threatening situations when aerospace critical components are processed. The proposed airborne acoustic emission (AAE) monitoring equipment is able to grasp even the slightest deviation from the optimum spray conditions occurring during spraying. This capability allows for instant response when an abnormal change in the process is recorded. This implies that the spray-coated parts can be protected and no extra time will be needed for salvage rework. Listening to the spray process and interpreting the acoustic emissions is a simple and cost-effective solution which will be easy to use and adopt.

At the moment, all spray monitoring systems (Spray-Watch by Osier, Accuraspray by Tecnar and others) are

✉ Spyros Kamnis
spyros@monitorcoatings.com

¹ Castolin Eutectic-Monitor Coatings Ltd,
Newcastle NE29 8SE, UK

² Department of Computer Science and Biomedical
Informatics, University of Thessaly, 35100 Lamia, Greece

³ Department of Materials, Loughborough University,
Loughborough LE11 3TU, UK

⁴ TRL9 Limited, Newcastle NE2 3AH, UK

static and they cannot be used when the torch is in motion. These systems are vital tools for design, process optimization and system calibration; however, they can only provide stagnant diagnosis of the spray process which is rarely the case in commercial applications. The current technology limitations in continuous monitoring of thermal spray processes have implications in global coating operations and quality assurance. For a long time, controlling a multitude of complex processes with precision into the supply chain has been a core research subject within the aerospace OEMs who apply surface modification techniques on critical engine parts. The use of a sophisticated and reliable continuous AAE monitoring technology will allow issues that affect coating quality, to be quickly identified and resolved centrally—even across global operations and into the supply chain.

Monitoring of HVOF Using Surface Contact Sensors

Research into acoustic emissions from the thermal spray process has primarily focused on the use of sensors in contact with the sprayed substrate to monitor the kinetic properties of particle deposition and the growth of coating defects such as cracks and delamination. For example, Faisal et al. (Ref 1) conducted successful experiments with a single contact sensor to measure the total kinetic energy of particles impacting the substrate. Crostack et al. (Ref 2) developed a model relating velocity and diameter of particles to acoustic emission amplitude. Lugscheider et al. (Ref 3) investigated the relationship between spray angle and acoustic emissions. Nishinoiri et al. (Ref 4) used a non-contact laser AE technique to monitor the formation of defects such as microfracture and delamination in coatings. These methods have shown promise in accurately monitoring the quality of thermal spray coatings as they are being sprayed, but the contact sensor must be carefully positioned on the substrate and calibrated for every part being sprayed. This drastically increases spraying time for each part and would necessitate training operators in the use of the monitoring equipment. These studies rely on the Raleigh waves on the substrate surface due to particle impact, whereas the current investigation focuses on the airborne acoustic emissions (sound) produced during the HVOF process.

Welding Monitoring Using Acoustic Emissions Technologies

Airborne acoustic emissions studies for thermal spray process monitoring are very limited; however, in other processes such as various welding processes (VPPAW, SMAW, laser welding) and machining processes, acoustic emissions are closely monitored and analyzed to give real-time predictions about certain aspects of the outcome of the

process, or health of the hardware in use. This method has attracted considerable research interest. Studies show that the acoustic signal acquired during the welding process can be used to monitor weld characteristics, such as penetration quality (Ref 5, 6), weld pool status (Ref 7), irregularities and stability (Ref 8) during the welding process. Detection of defects by acoustic signal analysis is based on the identification of the acoustic characteristics and understanding of several phenomena, such as weld pool oscillation behavior (Ref 9), arc plasma jet pulsation, change in arc intensity and metal transfer, which are the relevant sources of sound generated during the welding process.

In the literature, a variety of signal processing techniques, as well as neural networks and other methods, have been used to try and distinguish useful sound from background noise. Wang et al. (Ref 9) demonstrated the use of the short-time Fourier transform in detecting and locating irregularities on a weld bead. Wang and Zhao (Ref 5) used the variance of a segmented sound signal to monitor a keyhole opening. This feature was found to give a significant correlation with keyhole size, which can be utilized to monitor burn-through defects. Huang and Kovacevic (Ref 10) extracted the sound pressure deviation and band power from the acoustic signal and used them as the inputs of a neural network to establish the relation between acoustic signal and depth of penetration in laser welding. Saad et al. (Ref 7) calculated the power spectral density of the segmented sound signal acquired from the welding process and used it as an input for a neural network model to distinguish the keyhole mode from the cutting mode. Grad et al. (Ref 8) found that kurtosis (sharpness of a peak of a frequency distribution curve) of acquired sound signals can be used to monitor the stability of a welding process.

Thermal Spray and Sources of AAE

Thermal spraying encompasses a wide range of coating deposition processes with the common aspects that a feedstock, most commonly a powder, is partially melted by a supersonic flame (HVOF/HVAF) or plasma and propelled toward the substrate. These heated particles form splats on impact with the substrate, and the coating is built layer by layer. Important parameters of thermal spray processes include the powder feed rate, particle size, gas flow rates, fuel to oxygen ratio (in combustion thermal spray processes), nozzle geometry and standoff distance. Changes in these parameters will mean changes in the resultant airborne AE, due to changes in energy from the system being transformed into the acoustic emissions. The jet velocity fluctuations due to fluctuations in the combustion pressure are easily detectable due to overall decrease or increase of dB in the booth. In contrast, other process variables are more difficult to detect and classify. For example, increased or decreased

powder feed rates would mean more or less energy from the jet being transferred to the particles for their acceleration. These AAE variations are well hidden within a broad range of frequencies, and their acoustic signature cannot be discovered effortlessly. Furthermore, due to thermo-mechanically induced stresses, the outlet diameter of a copper nozzle may increase altering in this way the convergent–divergent pressure ratios and consequently altering the AAE signals. Regarding the supersonic jet noise itself, it can be monopole where there is fluctuation in mass flow, dipole on surfaces where the flow causes fluctuating pressure and quadrupole from turbulent wakes. In HVOF/HVAF supersonic jets, noise generated may be due to several reasons such as flow separation, incident turbulence, turbulent boundary layer and vortices in the wake region (Ref 11, 12).

Research Methodology

To assess the feasibility of this approach, a computational fluid dynamics model was developed early in the project aiming to simulate the gas flow and aeroacoustics of the process. The gas flow analysis revealed the strong influence that the PFR and SOD have on the gas dynamics of the HVOF torch. The initial results were acquired by conducting a basic aeroacoustics analysis. The power–frequency spectrum during HVOF was identified, and the distinguishable acoustic signatures were broadly categorized. The simulations revealed that the PFR and SOD dominant frequencies have their origin in different turbulent structures. As a consequence, the dimensionality of the problem is relatively low because the variables do not carry the same information. The decision to use a shallow neural network for process monitoring that could benefit from this condition was made based on the CFD preliminary results. Under different conditions, a more sophisticated deep learning algorithm and a larger dataset would be necessary to unveil the complex correlations hidden in overlapping data.

A series of experiments were then designed in an effort to create a clean dataset for artificial neural network (ANN) training. The selected target coating property in this study is the microhardness. Microhardness is a key coating property when high wear protection is required; however, other properties such as porosity, corrosion, decarburization and toughness may be equally important depending on the mode of operation. This approach could be applied to monitor these additional properties, provided that sufficient experimental data are available. The research approach flowchart is depicted in Fig. 1. The ANN model development is summarized in Fig. 2. The selection of inputs is a major first step toward a neural network with good generalization ability and accuracy. Instead of using unfiltered data in the network, some data cleaning was performed

aiming to improve the ANN training and testing accuracy. The first training dataset was devised under different PFR conditions and a fixed SOD. In this way, the power frequencies that carry input information were correlated to different PFRs. The highly correlated power frequencies were prioritized for later use in the final model. The second training dataset was prepared by altering the SOD at a fixed PFR. Similarly, the highly correlated power frequencies were selected as primary input to the final model. Finally, six frequency ranges for the PFR and four for the SOD were selected leading to a total of 10 power frequencies in the dataset. These ten inputs to the ANN model were selected for continuous monitoring, and their correlation to the coating microhardness was assessed. The selected inputs in the form of power–frequency range carry information related to the SOD and PFR. In this way, the accuracy of the monitoring process can be maintained when the PFR and SOD are altered during spray.

Acoustic Modeling of HVOF thermal spray process

Geometry Model and Flow Domain Discretization

The studied spray torch is represented schematically in Fig. 3. Fuel, oxygen and air are injected into the combustion chamber, where the fuel burns and the combustion products are accelerated downstream through the convergent–divergent nozzle. For the present analysis, the nozzle configuration comprises of an inlet throat diameter of 5.5 mm, 26 mm divergent length and outlet throat diameter of 7.5 mm. Fine meshes are employed to the sensitive areas such as the nozzle entrance and exit, the barrel exit and the free jet centerline where high flow gradients are expected and increased accuracy is required. The governing equations of flow and acoustics are solved over the grid developed using the program Ansys FLUENT 19 Academic Edition (Ref 13). The location of the sensor in the computational domain is shown in Fig. 1. The same microphone location was used during the experimental acquisition of the acoustic signals. The coordinates from the nozzle exit are 0.055 m (x), 0.025 m (y) and 0 m (z).

Solver Settings and Boundary Conditions

The phenomena associated with sounds can be understood and analyzed in the general framework of fluid dynamics. ANSYS Fluent offers a method based on the Ffowcs Williams and Hawkings (FW-H) formulation (Ref 14). The FW-H formulation adopts the most general form of Lighthill's acoustic analogy and is capable of predicting sound generated by equivalent acoustic sources. The solver

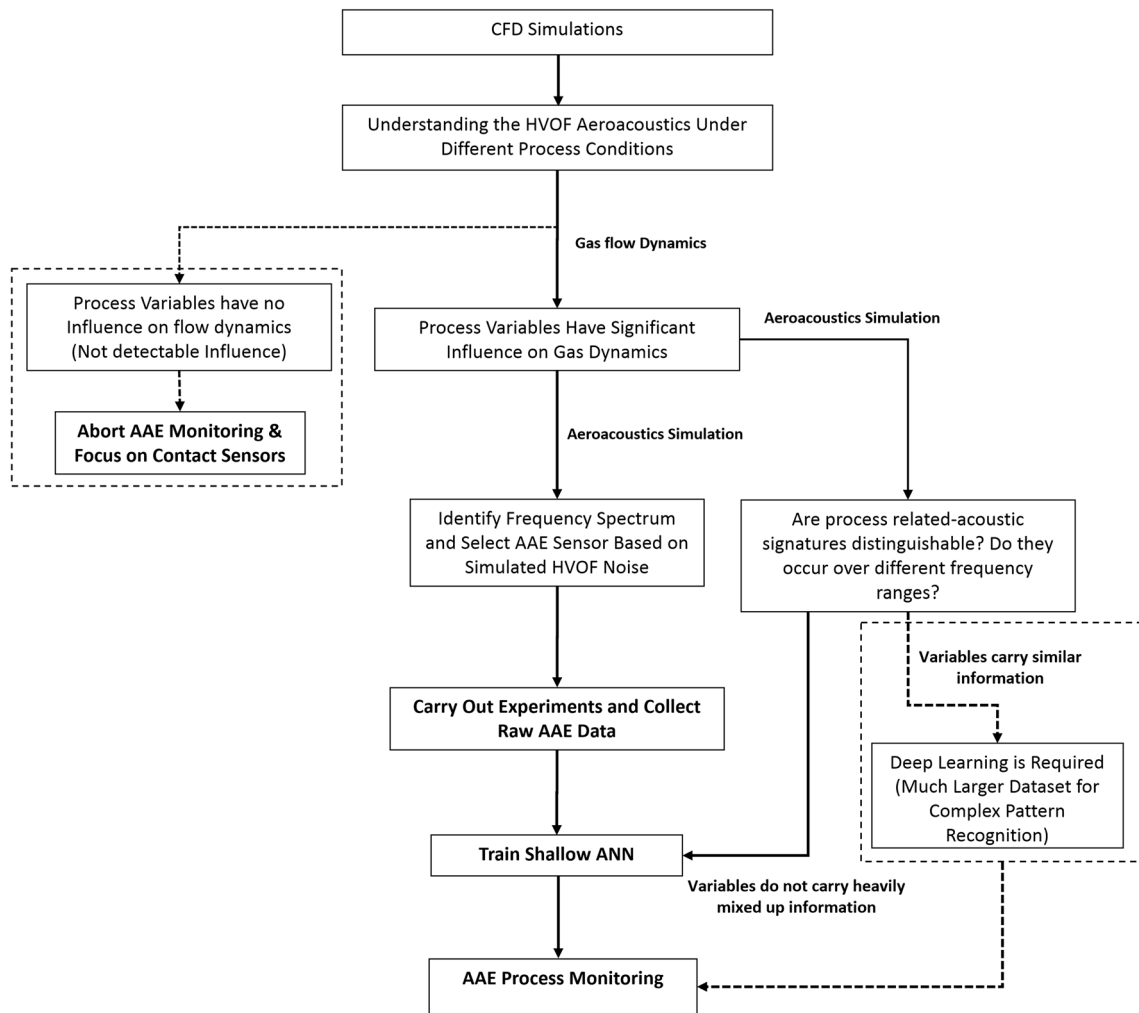


Fig. 1 Research approach diagram

adopts a time domain integral formulation, wherein time histories of sound pressure, or acoustic signals, at prescribed receiver locations are directly computed by evaluating corresponding surface integrals. It is out of this work’s scope to probe into the mathematics of the modeling work. The authors have carried out extensive modeling and simulation work in the field of HVOF thermal spray, and several validation data can be found in (Ref 11, 12). The current model predictions are validated against experimental data in Sect. 6.1. The detailed model setup parameters are summarized in Table 1.

Neural Network Data Modeling

In their main embodiment, artificial neural networks are nonparametric methods used for pattern recognition inside large datasets. They generate an outcome based on a weighted sum of inputs which is afterward passed through an activation function. The activation function defines the

output from the neuron in terms of its combination. Three of the most used are the logistic, the hyperbolic tangent and the linear functions. In this study, the logistic function has been used with a sigmoid shape. This activation is a monotonous crescent function which exhibits a good balance between a linear and a nonlinear behavior. A detailed description of perceptron theory, the main component of neural networks, can be found in the Neural Designer software online manual by Artificial Intelligence Techniques Ltd (Ref 20). Of all artificial neural network types used in classification matters, a viable option is the multilayer perceptron (MLP) which is organized in three types of layers: an input layer, hidden layers (usually not more than three) and an output layer.

Artificial Neural Network Training

For this analysis, a multilayer perceptron was used to model the AAE data from the HVOF process at Monitor Coatings-Castolin Eutectic in the UK. Although the

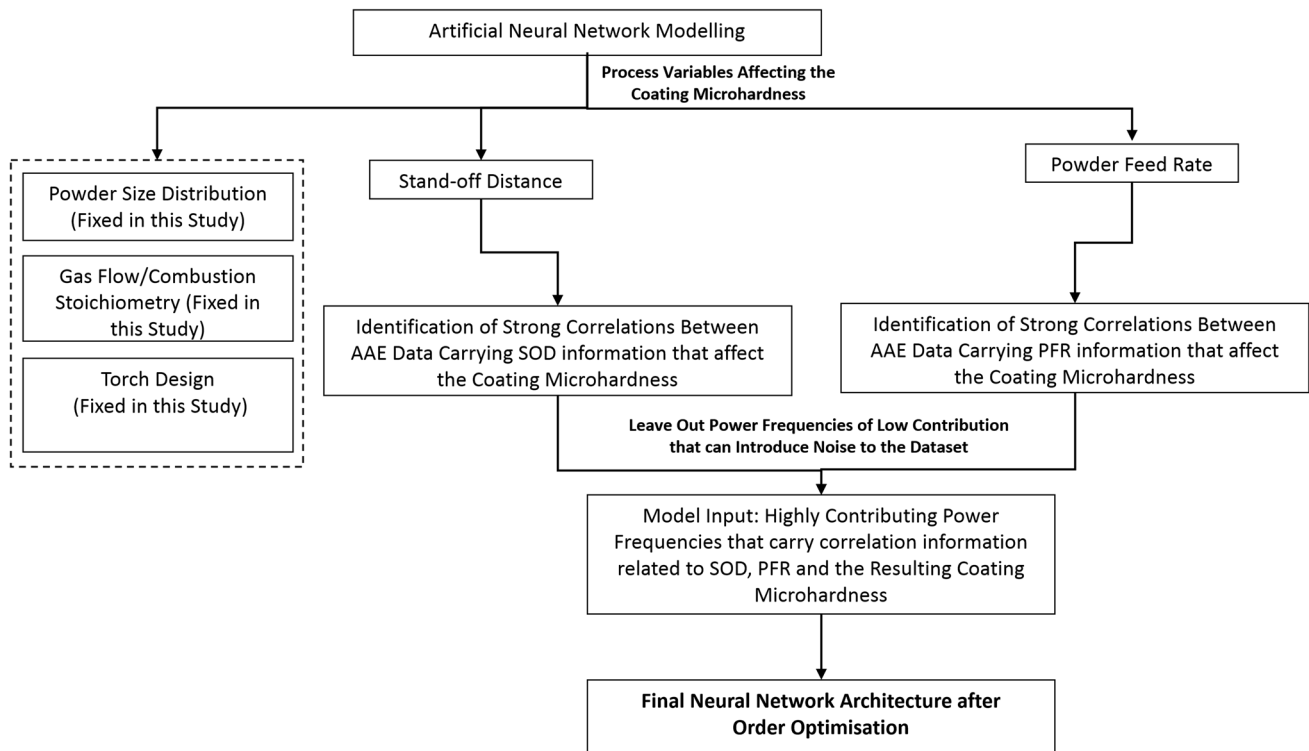


Fig. 2 Artificial neural network model setup

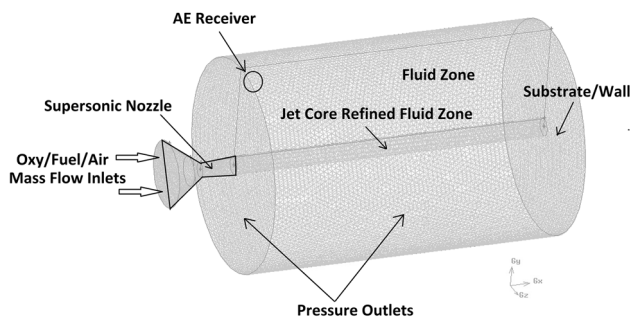


Fig. 3 Computational fluid dynamics domain and boundary conditions

number of hidden layers generally ranges between one and three, previous studies (Ref 21) have shown that ANNs with a single hidden layer can estimate any differentiable

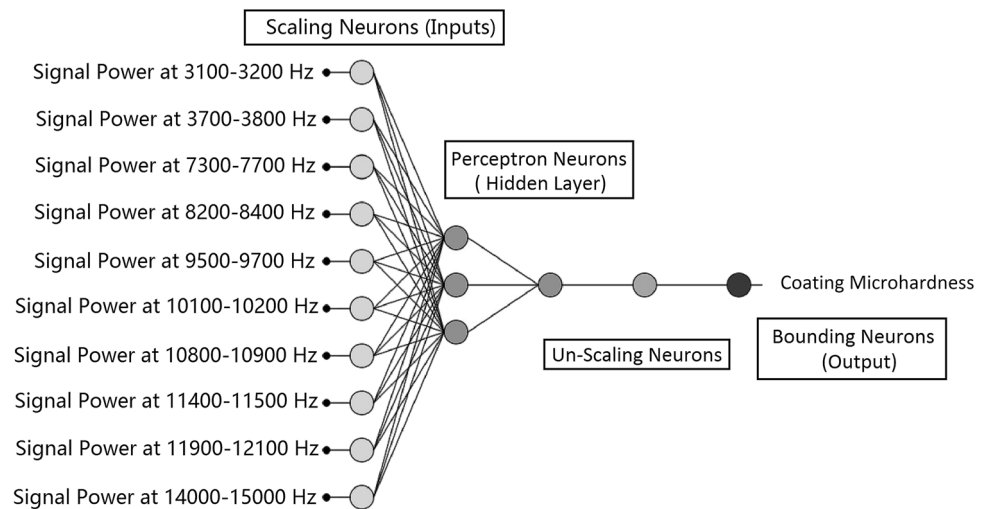
function, provided that they have enough hidden units. Moreover, a high number of layers would significantly increase the processing time and the adjustments required during network training. The number of nodes in the hidden layer was varied between a minimum of three units and a maximum of 10 units. The analysis employed a total number of 10 input nodes corresponding to the spectral density of dominant frequencies when the spray distance and powder feed rate were altered during spray. The gas flows were fixed corresponding to maximum coating microhardness achieved at 100 mm SOD and 1 kg/h powder feed rate.

The weights were initialized using a uniform distribution within $[-0.5, 0.5]$ range. Afterward, these were adjusted using the gradient descent method with momentum rate and learning rate set equal to 0.1. The training was

Table 1 Aeroacoustics model setup

Solver (Ansys 19)	3D-Transient	Second-order explicit-coupled, compressible with a fixed 10^{-7} -time step	Ref [12]
Turbulence	LES	Smarwoski-Lilly	Ref [15]
Combustion	Species/transport	Eddy dissipation	Ref [11, 12, 16]
Acoustics	FW-H	90° to nozzle exit	Ref [14]
DPM	Random walk model particle density: 5000 kg/m^3	Particle size: $10 \times 10^{-6} \text{ m}$	Ref [17-19]

Fig. 4 Neural network architecture used to predict the coating microhardness as a function of frequency power inputs



terminated when one of the stopping criteria was reached: a maximum number of 1000 of iterations and a variation in the average error below 0.001 for 10 consecutive cycles. The training was performed in a “batch” mode, meaning that weights were adjusted only after presenting all training records to the network. To reach a final approximation model, several cycles (epochs) were performed until meeting the aforementioned stopping conditions. Out of the 100 neural networks trained, the best in term of detection rates on the test set was retained. The selected neural network architecture shown in Fig. 4 is a multilayer perceptron (MLP 10-3-1) for the prediction of microhardness, containing ten nodes in the input layer, three nodes in the hidden layer and one output node. The evolution of the training set error was compared with the evolution of the validation error in order to make sure that the final model is not over-fitted, a characteristic that reduces the generalization capacity of the model when tested on new data. The ANN model setup is shown in Table 2.

Table 2 Artificial neural network model parameters

Scaling method	Mean standard deviation (Ref 22)
Un-scaling method	Mean standard deviation (Ref 23)
Bounding layer	Yes
Error method	Normalized squared error
Training algorithm	Gradient descent (Ref 22-24)
Activation function	Hyperbolic tangent (Ref 22)
Output layer function	Linear (Ref 22, 23, 25)

Experimental Apparatus

The acoustic emission monitoring apparatus comprises a single microphone with a preamplifier in an industrial thermal spray booth, a signal conditioning unit and a PC for data processing.

Acoustic Signal Acquisition

The microphone was a 1/2" random incidence, high frequency, high amplitude, prepolarized microphone and preamplifier system. The microphone has a frequency range from 4 Hz to 25 kHz and distortion limit of 160 dB with a noise floor of 19 dBA. It was calibrated to compensate for the effect of its own presence in the acoustic field generated in the experiments. The microphone system was 77 mm in length with a fitted grid of 13 mm diameter and was kept in a fixed position in the coating chamber behind a microphone windshield during spraying. The experiments were carried out using the above data acquisition setup (Fig. 5) to monitor an HVOF system developed by Castolin Eutectic-Monitor Coatings Ltd in the UK (Ref 26, 27).

Equipment and Experimental Process

A commercially available agglomerate sintered powder of WC- 17Co mass fraction (H.C Starck, AMPERIT 526) (Ref 27) was used for the deposition of coatings. The detailed chemical composition and size distribution of the powder are presented in (Ref 28). The powder used shows the median size to equal about 18.9 μm. The measured particle size distribution ranges from 12.5 μm to 28.1 μm at 10% and 90% of the cumulative, respectively.

The coatings were deposited onto steel substrates. The substrates were grit blasted with 46 μm alumina particles at

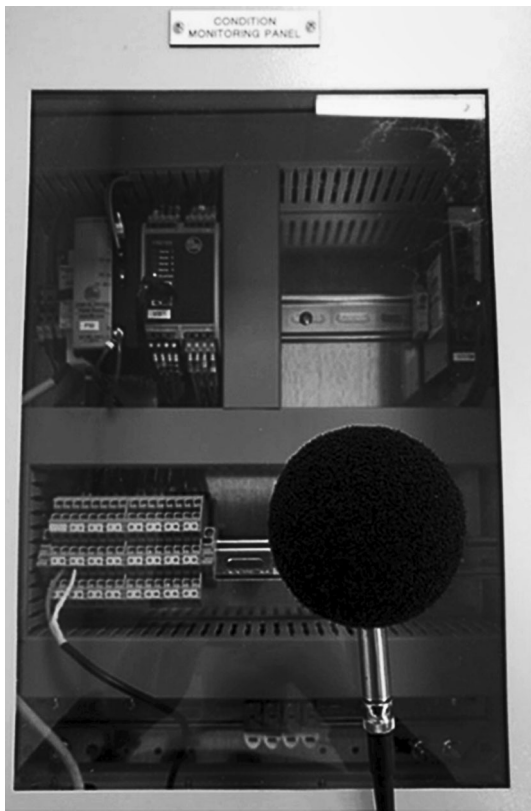


Fig. 5 Signal acquisition unit and microphone used in this investigation by IFM electronics Ltd

a distance of 100 mm; subsequently, they were blasted with high-pressure air and mechanically cleaned to remove any remaining grit on the surface. The samples were sprayed using Castolin Eutectic-Monitor Coatings (UK) HVOF torch which has been designed and built in-house. The process parameters for the gun were previously optimized in-house using Oseir's SprayWatch system for achieving the best microstructure, the highest microhardness and optimum deposition conditions (Ref 26, 27).

The experiments were performed with the HVOF gun traversing linearly over the substrates using a robotic arm. The spray angle was fixed at 90 degrees, while the SODs and powder feed rates were altered and individually controlled. This allowed for studying the influence of each one on the generated acoustic signals inside the spray booth, while all other parameters were held constant. The increments in spray SODs were 100 mm, 110 mm, 120 mm, 130 mm and 140 mm. The powder feed rates were varying from 0.2 kg/h to 2 kg/h at 0.2 kg/h increments for each individual SOD. Thus, 50 combinations of SOD and PFR values were considered and an equal number of acoustic signals were acquired.

Post spray, the samples were cut and polished following a routine developed to minimize and carbide pull-outs during polishing substituting the final stages of diamond

polish with silica abrasive of 40 nm. Cross sections of the samples were examined under the Optical Microscope at Monitor Coatings. The equipment is calibrated regularly as per Monitor's aerospace NADCAP accreditation requirements. The microhardness was examined with a Vickers micro indenter (Future Tech, FM-100) under a load of 300 g (HV0.3). Ten measurements were taken per sample.

For the implementation of a prototype active monitoring system, it was decided that the unit should be able to notify the operator in real time. For this purpose, a preinstalled MATLAB application has been used in conjunction with the VSE001 (IFM electronics (Ref 29)) signal conditioning unit (Fig. 5) to monitor the important frequency ranges that were identified and validated in the experimental program. These frequency ranges were used to set signal power thresholds which, when crossed, trigger an alarm suggesting a fault in the spray process.

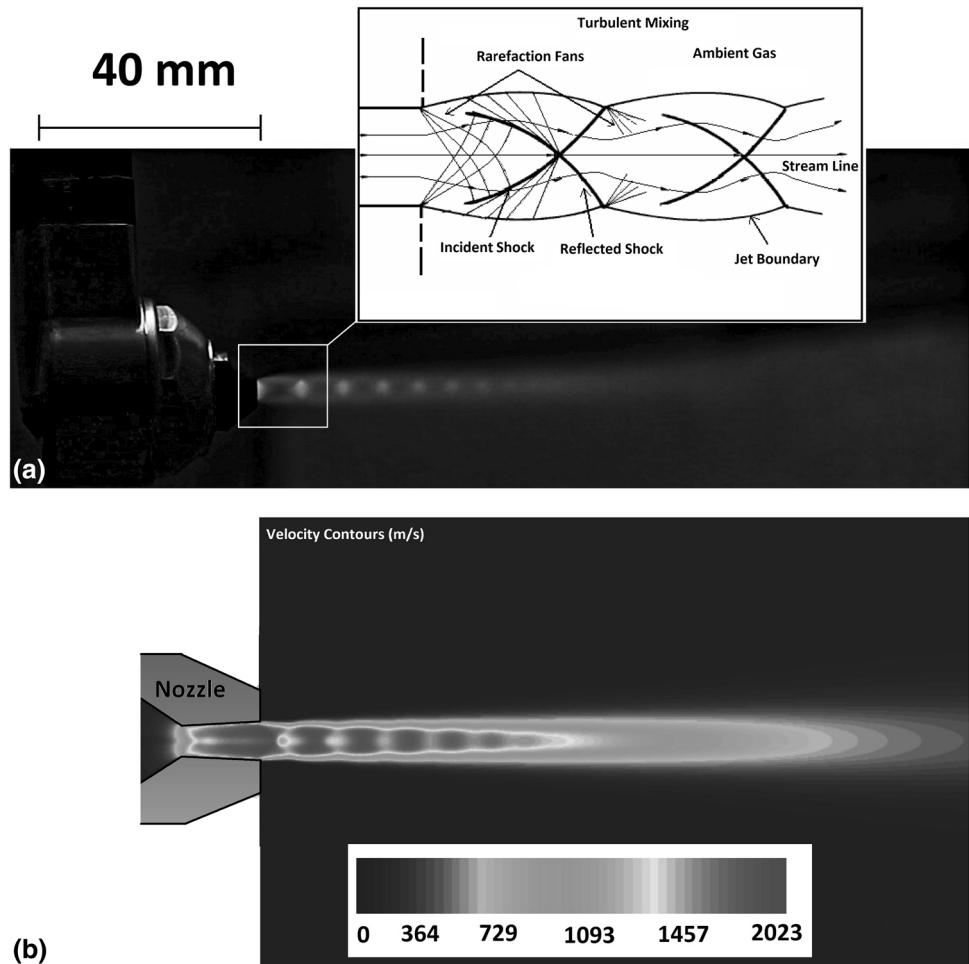
Results and Discussions

The modeling work focuses on the airborne acoustic signal acquisition when thermal spray powder is injected axially in the supersonic jet. High particle concentration in the flame results in strong coupling between the solid and fluid phases when the Strouhal number is > 10 . The flame temperature drops, and the momentum transfer from the high energetic flame to the particles leads to jet velocity profile alteration both in the axial and the radial directions. It is expected these multiphase interactions to have an impact on the acoustic footprint of the process; however, it is unknown if the particle–flame interactions are detectable and over which frequency and spectral density range detection may occur. The underlying physics of this process are not well documented in the literature, and our intention is to probe into this HVOF spray characteristic. In this study, the aeroacoustics modeling work has been validated by comparing the experimental and modeling signal Fourier transforms.

Fluid Flow and Aeroacoustics

The complicated structure of the supersonic jet (Ref 30) is shown in Fig. 6. First, the jet boundary oscillates as the jet gas periodically over expands and converges in its attempt to match the ambient pressure. The gas continually overshoots the equilibrium position because the effects of the boundary are communicated to the interior of the jet by sound waves, which, by definition, travel more slowly than the bulk supersonic flow. The characteristic paths of the sound waves converge to form the second feature of the jet, the network of crisscrossed shock waves or shock diamonds. These standing shocks alternate with rarefaction

Fig. 6 (a) Image showing the experimental supersonic jet expansion (b) velocity contours of the simulated supersonic jet expansion



fans. The gas in the jet interior expands and cools down as it flows through the rarefaction fans and is compressed as it passes through the shock diamonds. The jet structure shown in Fig. 6(a) and (b) in reality does not have sharp, stable boundaries but turbulent boundaries, where jet and ambient gases mix. Near the orifice, where the pressure mismatch is large, Mach reflections occur, but further downstream the reflections are regular. The mixing layer which grows eats its way into the supersonic core of the jet. When the mixing layer reaches the axis of the jet the flow is subsonic and fully turbulent. Large and small eddies are formed in the shear layer of the gas jet. These eddies are very small in size near the nozzle exit where they originally form, and then become larger downstream until full dissipation. Ultimately, the formation, propagation and dissipation of eddies result in the jet noise.

When the powder is introduced into the flame at 5 kg/h feed rate, the mean velocity profile is affected as depicted in Fig. 7. To demonstrate this behavior, we provide the evolution of the radial velocity profile of the gas in several different axial locations in the external flow field with and without powder in the jet. These locations are based on the

distance from the exit of the HVOF torch. It is clearly seen that the centerline velocity decays along the axial direction faster in the presence of the discrete phase and the jet propagates outwards in the radial direction (Fig. 7b, d, e). At larger standoff distance ($x = 80$ mm from the nozzle exit), the velocity at the jet core is nearly half compared to the powder free jet. Turbulent mixing with the ambient air occurs faster attributed to the jet kinetic energy being transferred to the particles during inflight acceleration. While the velocity slows down in the centerline, the boundaries of the jet are thrust outwards as the flow is blocked by the particle cloud confined in the axis of the jet as shown in Fig. 7(a). Several studies (Ref 31-33) have demonstrated the effect of supersonic jet diameter in the aeroacoustics. Typically, a wider jet creates a shift in frequencies where energy peaks occur. This is more evident in the high-frequency range where the signal contribution originates from the small highly energetic turbulent eddies occurring near the nozzle exit at the jet-ambient gas boundary. The observed faster velocity dissipation is expected to alter the formation of large eddies downstream, contributing to the low-frequency range as well. The

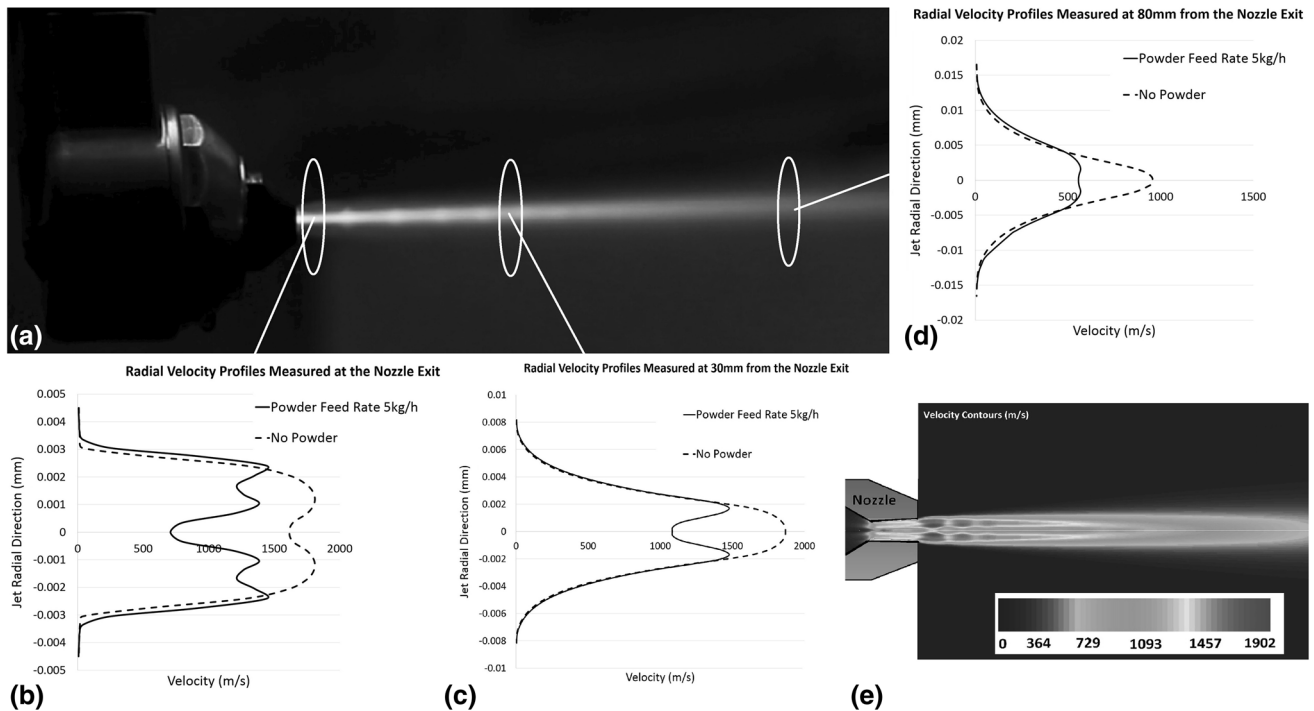
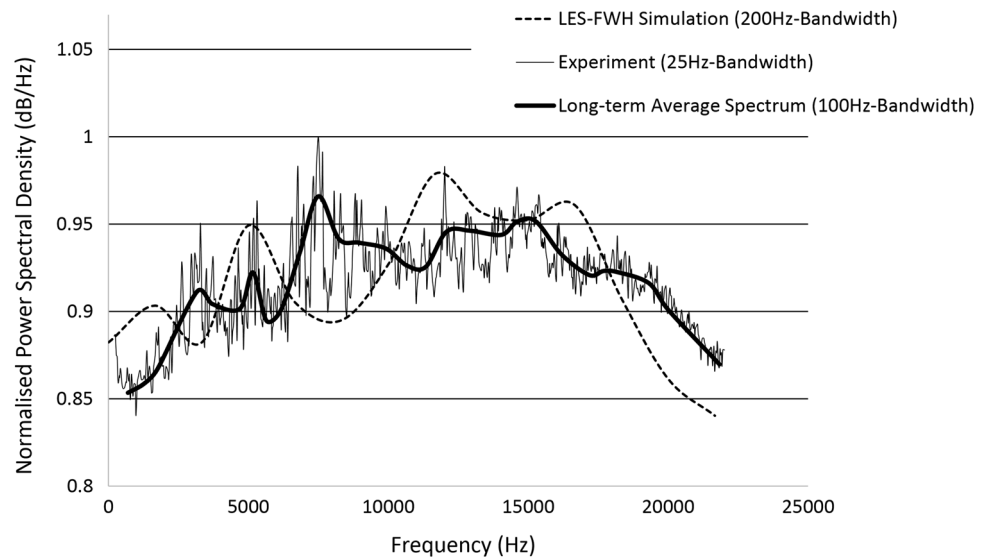


Fig. 7 (a) Image showing the powder traveling through the centerline of the supersonic jet, (b) radial gas velocity profile at the nozzle exit, (c) radial gas velocity profile 30 mm downstream, (d) radial gas velocity profile 80 mm downstream, (e) velocity contours with 5 kg/h powder feed rate

Fig. 8 Time average spectrogram showing the experimental and numerical noise acquisition without a substrate and powder in the flame. The bold solid line shows the experimental spectrogram after 100 Hz bandwidth and 10 s time averaging



modeling results suggest that an overall frequency shift of the noise peaks should be expected due to the particle laden flow in the jet and the consequent velocity profile alterations.

The large eddy simulation predictions, coupled with the FW-H noise model approach (Fig. 8), show a similar trend as that measured experimentally. This means that the nature of the non-uniform quadrupole orientation is captured well by the CFD simulations. The noise predictions are

found to be in good, but not perfect, agreement with the experimental data. As expected, we have underpredicted the noise level at high frequencies. This is due to the small turbulent structures of the jet which are not resolved by our mesh. However, in general, the LES-FW-H approach demonstrates the ability to capture the spectra shape correctly. More specifically, the predicted power spectral density is lower in the low-frequency range, higher in mid-frequencies and lower over higher frequencies. The model

accuracy can be improved by reducing the simulation time step, increasing the simulation overall time and by refining the mesh; however, this would require several months of computational effort since the aeroacoustics, turbulent combustion, compressible supersonic flow and discrete phases are solved simultaneously in a 3-D space.

A large amount of experimental evidence suggests that acoustic waves are strongly coupled to many mechanisms encountered in turbulent flows. The free shear layers are especially sensitive to acoustic waves (Ref 34). This interaction may lead to large flow instabilities; therefore, it is important to avoid artificial free boundary reflection of the acoustic waves. To overcome this issue, we damp reflected waves by numerical viscosity, using a coarse mesh near the outlet boundaries (buffer zones). Although this approach is effective for the elimination of reflected waves, a coarse mesh may result in localized numerical resolution reduction responsible for the over predicted noise at the very low-frequency range as shown in Fig. 8. Another distinctive feature of the process is the fragmentation of power peaks over a range of frequencies. At the early stages of this work, the numerical approach revealed that we should be looking for energy–frequency pairs rather than maximum or minimum amplitude over the full range of frequencies. The same behavior was later observed experimentally when the powder feed rates were altered from low (1 kg/h) to high (4 kg/h) as shown in Fig. 9. At high feed rates, the power spectral density is lower over the frequency range up to 5000 Hz. The peak power is observed at 15,000 Hz, while for the low powder loading occurs at 5,000 Hz. This is in line with the fluid flow (Fig. 7) and aeroacoustics modeling results (Fig. 9) suggesting a jet shape change due to faster decay of the jet core and the small jet diameter increase when powder is present in the flame. A clearer shift of the power peaks to

the lower-frequency range is observed when the jet hits a substrate at short standoff distances as shown in Fig. 10. At 80 mm from the nozzle tip, the jet experiences a rapid deceleration upon impact creating large circulation zones (vortex-induced zone) near the substrate. These large turbulent structures give rise to the low-frequency power spectrum. This effect dominates over the upstream shear layer mixing noise. Moving the substrate to 120 mm from the nozzle allows for more canonical jet decay, where mixing layer structures at the mid-frequency range dominate the noise generation process.

When thermal spray phenomena are examined in isolation, the interpretation of the dataset is straightforward. However, the increased complexity of data handling and interpretation can be realized when the problem is grounded to reality where the above spray conditions are combined introducing variable SOD, feed rates and particle substrate impact noise to the spray process. A powerful instrument for disentangling the complexity of their subject matter is required, especially when we do not possess a clear knowledge of the dynamical relationships among these spray factors and the resulting acoustic signals. In this context, ANNs can help to identify the possible causes and their peculiar combination linked to the onset of a certain coating property by analyzing the acoustic signals.

Experimental Acoustic Data Modeling

In this section, we introduce a neural network model for the analysis of the experimental data with the aim of finding fundamental relationships between the target coating properties and the emitted acoustic signals during spray. The ten power–frequency ranges shown in Table 3 (Column 3 to Column 12) are the 10 down selected power frequencies as detailed in Sect. 2 having had the leave-out

Fig. 9 Time average spectrogram showing the experimental and numerical noise acquisition at different powder feed rates and without a substrate. Experimental spectrogram at 100 Hz incremental bandwidth and 10 s time averaging

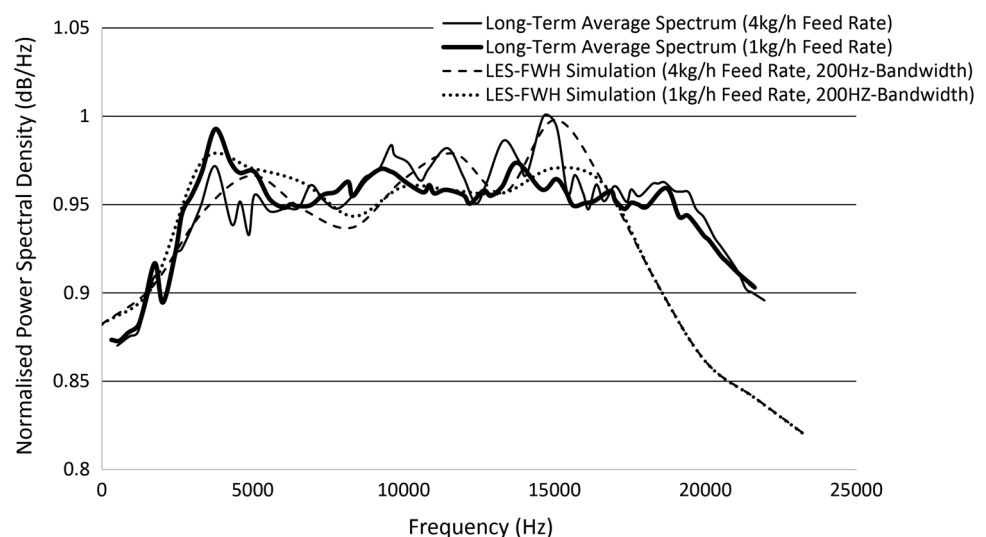
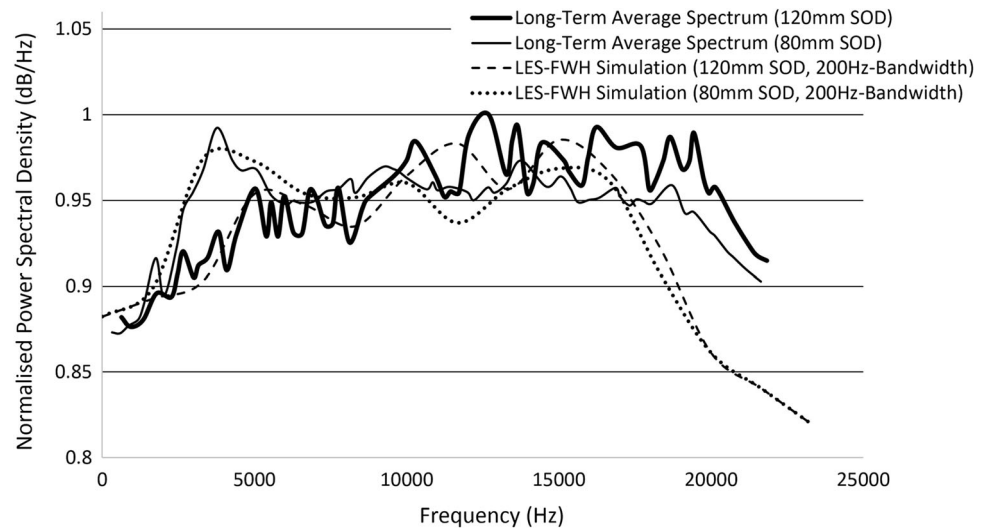


Fig. 10 Time average spectrogram showing the experimental and numerical noise acquisition at different substrate standoff distances and fixed powder feed rate. Experimental spectrogram at 100 Hz incremental bandwidth and 10 s time averaging



technique applied and having discarded the unwanted frequencies. The feature vector comprises of six peak power frequencies highly correlated to PFR (3100–3200 Hz, 14,000–15,000 Hz, 3700–3800 Hz, 7300–7700 Hz, 10,100–10,200 Hz and 10,800–10,900 Hz) and four peak power frequencies carrying information predominantly for the SOD (8200–8400 Hz, 7300–7700 Hz, 11,900–2100 Hz, 9500–9700 Hz.). The dataset of the 50 experiments/instances that were described in “Equipment and Experimental Process” was randomly split into 40 training and 10 testing/validation dataset, of size equal to 40 and 10, respectively.

Correlation Ratios of PFR Within the Selected Frequency Bands

A training strategy was applied to the neural network in order to obtain the lowest possible loss. Loss value implies how well or poorly a certain model behaves after each iteration of optimization. The accuracy of a model is determined after the model parameters are learned. The test samples (data that were not used to train the ANN) are fed to the model, and the number of mistakes the model makes is recorded, after comparison to the true values. Then, the percentage of misclassification is calculated. The type of training is determined by the way in which the adjustment of the parameters in the neural network takes place. In this study, the quasi-Newton method is applied to adjust the network weights in order to minimize the error (loss) function. This method is based on Newton’s method, but does not require calculation of second derivatives; instead, it computes an approximation of the inverse Hessian at each iteration of the algorithm, by only using gradient information. As shown in Fig. 11(a), the initial value of the training loss was 13.8196%, and the final value after 333

iterations was 0.00501855%. The initial value of the validation loss was 15.0176%, and the final value after 333 iterations was 0.922464%. The very low validation error implies that the model can generalize to unseen data and can distinguish between PFR and SOD contributions when the information coexists in the dataset.

To further assess the model accuracy, a standard linear regression analysis was carried out (Fig. 11b) between the scaled neural network outputs and the corresponding targets for the independent testing/validation subset and three parameters indicating the quality of the regression were calculated. The first two parameters correspond to the y-intercept and the slope of the best linear regression relating scaled outputs and targets. The third parameter is the correlation coefficient between the scaled outputs and the targets (Ref 35). For a perfect fit (outputs exactly equal to targets), the slope would be 1, the y-intercept would be 0, and the correlation coefficient is equal to 1. Figure 11(b) illustrates the linear regression for the scaled output powder feed rate (PFR). The predicted values are plotted versus the actual ones as squares. The black line indicates the best linear fit (0.8 for this model). The gray line indicates a perfect fit. A graphical representation of the network architecture is depicted in Fig. 11(c). The number of inputs is 10, the number of outputs is 1, and the single hidden layer contains five neurons.

The dominant power peak frequencies that are highly correlated to PFR were determined without any information related to the SOD. For this reason, it is necessary to assess if the highly correlated frequencies remain linked to PFR when SOD dominated frequencies are introduced to the dataset. This task is executed by removing one input at a time. This shows which input has more influence in the selected output. Figure 11(d) shows the importance of each input. If the importance takes a value greater than 1 for an

Table 3 Data matrix for developing the artificial neural network model

	Column 1	Column 2	Column 3	...	Column 12	Column 13
Row 1	Powder feed rate (kg/h)	Standoff distance (mm)	Normalized peak power spectral density (dB/Hz) at frequency range 3000-3200 Hz	...	Normalized peak power spectral density (dB/Hz) at frequency range 14,000-15000 Hz	Coating microhardness (HV0.3 kg)
Row 2	0.2	100	0.36	...	0.72	1300
Row 3	0.4	100	0.37	...	0.68	1310
...
Row 51	2	140	0.48	...	0.99	1030

input, it means that the testing/validation error without that input is greater than with it. In the case where the importance is lower than 1, the testing/validation error is lower without using that input. Finally, if the importance is 1, there is no difference between using the current input and not using it. The most important variable is the power peak at 3100-3200 Hz range that gets a contribution of 2.89 to the outputs followed by the peak power in the range of 14,000-15,000 Hz with the second larger contribution of 1.57. The results confirm that high correlation is maintained when the dataset is jeopardized with irrelevant information (SOD in this case). Furthermore, the results are in line with the observations in Sect. 6.1, suggesting that the powder feed rate would affect the jet shape promoting fast decay of the jet. The high frequency relates to the shear layer mixing and the low frequencies are affected by the large eddies at the jet core mixing region. As expected, the power change in mid-frequency range is less important (contribution close to 1) when considering PFR alone.

Correlation Ratios of SOD Within the Selected Frequency Bands

The same approach has been used to identify the correlation between the SOD and peak power frequencies when PFR-related information is included in the neural network. Figure 12(a) illustrates the training strategy losses in each iteration. The initial value of the training loss was considerably lower at 0.0578946, and the final value after three iterations was 0.0578836. The initial value of the testing/validation loss was 0.0382135, and the final value after three iterations was 0.0382130. The training strategy was implemented sequentially resulting in a much faster network training. From the linear regression analysis (Fig. 12b) of the scaled standoff distance (SOD) output, a better linear fit was achieved (0.95), indicating that the signals contain stronger information related to the spray distance as opposed to powder feed rates. The predictive neural network architecture was refined in order to minimize the model loss and is shown in Fig. 12(c). The number of inputs is 10, and the number of outputs (SOD) is 1. The complexity, represented by the numbers of hidden neurons, is 7, and the architecture of this neural network can be written as 10:7:1. The size of the scaling layer is 10, and the scaling method used for this layer is the mean standard deviation.

From the calculation of the testing/validation loss when removing one input at a time, the most important variable is the peak power at 8200-8400 Hz that gets a contribution of 6.2 to the outputs. The results confirm that the strong correlation has been maintained after the inclusion of PFR-related frequencies in the dataset. It is evident from Fig. 12(d) that the frequency range of interest has now

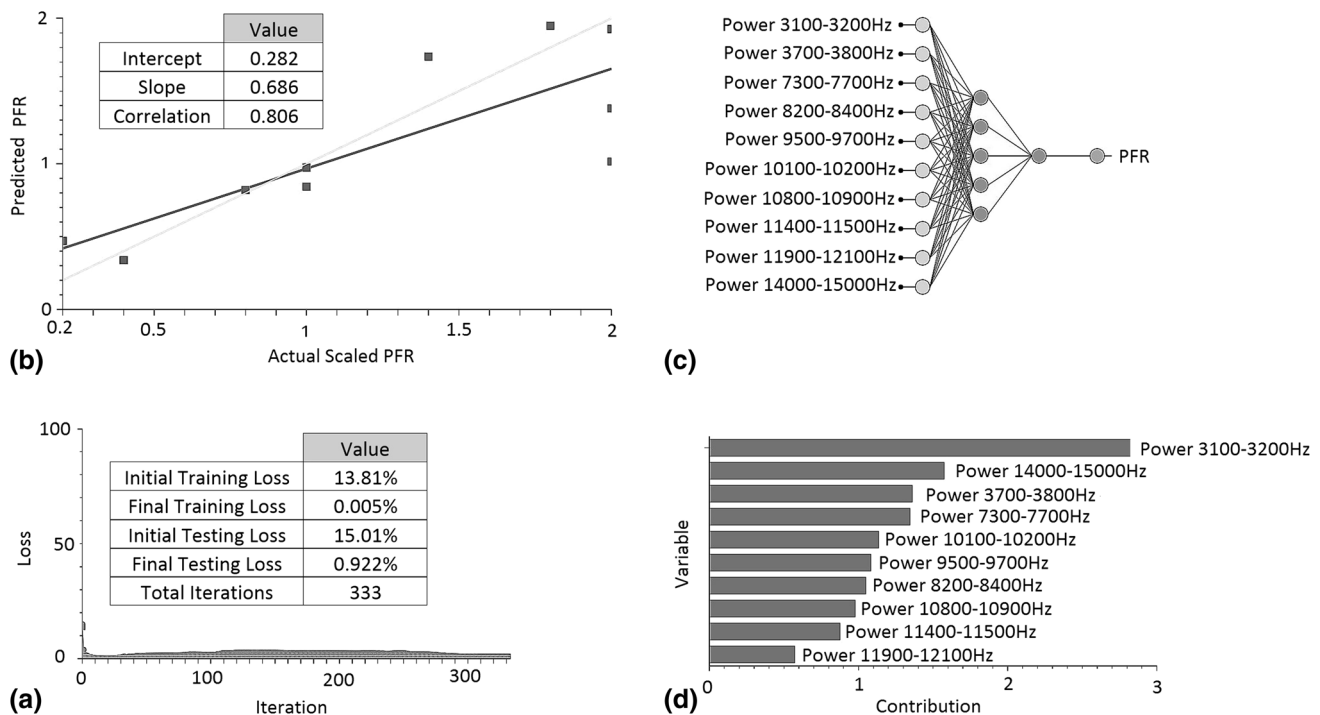


Fig. 11 (a) Error calculations, (b) linear regression analysis, (c) ANN architecture, (d) rating of input contribution to the outcome powder feed rate (PFR)

moved to the low–mid-frequency range as opposed to powder feed rate frequency range. The same has been observed in Fig. 10 where most power peak changes occur between 3000 and 10,000 Hz. Altering the position of the substrate opposite to the gun results in the creation of large vortex-induced zones near the substrate. These large turbulent structures give rise to the low-frequency power spectrum. This effect dominates over the upstream shear layer mixing noise.

Final ANN Model Accounting for Combined Influences on Target Microhardness

In the final stage, we can reconstruct the target, which is the coating property, by introducing the microhardness data for all instances under study. The preliminary analysis demonstrated that the input power frequencies are highly correlated to selected targets (powder feed rate and SOD). These correlations occur over different frequency ranges, indicating that these variables do not carry the same information and the ANN model shall benefit from their joint consideration. If the correlation rates were high over the same frequency range would mean that the PFR and SOD variables carry the same information from which the ANN model would not benefit introducing errors to the prediction of the coating microhardness when both spray inputs vary.

The linear regression parameter for the scaled output coating microhardness is illustrated in Fig. 13(a). The intercept, slope and correlation are very similar to 0, 1 and 1, respectively, suggesting that the neural network is predicting the testing data well. The overall model accuracy is within 3% implying that in terms of coating microhardness the predictions may oscillate with a maximum deviation close to 30 HV0.3. The final number of layers in the neural network is 2, and the architecture of this neural network can be written as 10:3:1 as shown in Fig. 13(b). The input importance analysis suggests that the most important input is in the range of 3100–3800 Hz that gets an average contribution of 3 to the outputs. This is the low-frequency range mainly associated with large eddies and the impact of the jet on the substrate. As expected, the effect of SOD on the coating microhardness is known to be larger compared to the effect of small changes in the PFR.

The results suggest that there is strong combined influence when varying the SOD and PFR; thus, at least 10 frequency ranges should be monitored simultaneously in order to get accurate prediction of the coating microhardness during spray. This is more evident when examining how the outputs vary as a function of a single input, when all the others are fixed. This can be seen as the cut of the neural network model along some input direction and through some reference point. For the four predominant power peak frequencies, the directional outputs are illustrated in Fig. 14.

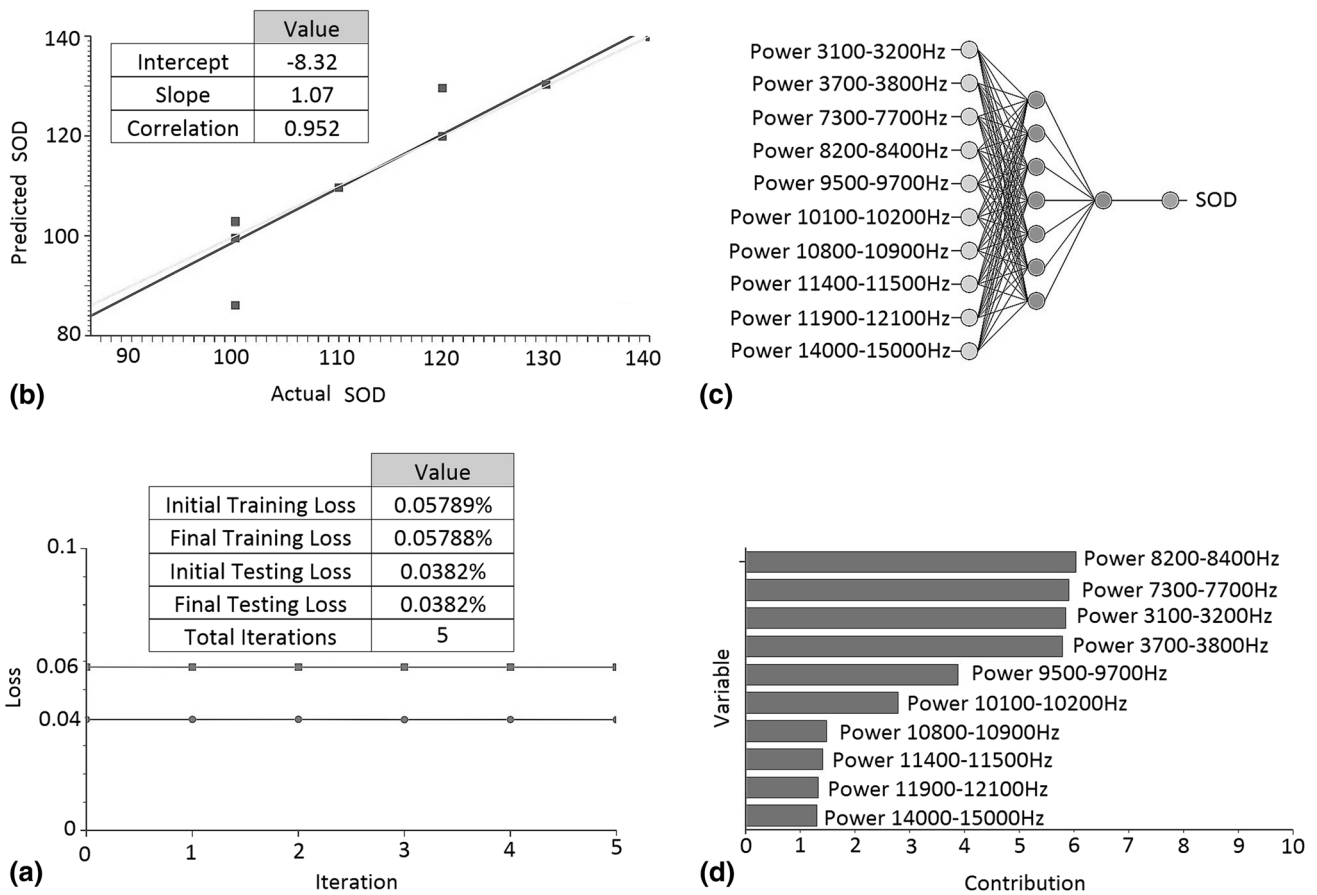


Fig. 12 (a) Error calculations, (b) linear regression analysis, (c) ANN architecture, (d) rating of input contribution to the outcome standoff distance (SOD)

These plots show the output coating microhardness as a function of the input power at 3100–3200 Hz, 3700–3800 Hz, 8200–8400 Hz and 7300–7700 Hz. The x and y axes are defined by the range of peak power at a given frequency range and the coating microhardness, respectively. For example, in the 3100–3200 Hz range the high-power values indicate lower coating quality as opposed to the 8200–8400 Hz range where coating quality increases with power. The resulting noise power levels contain information of both the PFR and the SOD which are not given as an input to the model. During spray, both parameters may change due to operational errors or as part of the spray process planning. For this reason, the predictive algorithm should be able to provide the key target output under any spray condition irrespectively.

The predictive ability of the developed ANN is further demonstrated in Fig. 15. This is the inverse of the ANN architecture shown in Fig. 13(b). The algorithm was tested against experimental data that were removed from the training dataset (unseen data). The single model input is the desired coating microhardness, and the target values are the average power peaks in three dominant frequencies as

described earlier. The powder feed rate was kept constant at 2 kg/h, and the standoff distance was fixed at 120 mm. Very good agreement has been observed in all frequencies. The largest deviation from the experimental data was found at the lower-frequency range where noisy data originate from the Rayleigh–Taylor instabilities that are responsible for the axisymmetric shedding of the jet. The accuracy and predictive capability of the model in unseen data is very promising and can pave the way for dynamic control of the process by iterative corrective intervention through the gas control unit and the robotic arm. This will require larger datasets and more advanced machine learning algorithms. Corrective actions may include increase or decrease in the gas flow rates, flame temperature control through stoichiometric ratio adaptations and adjustment of the SOD to achieve the desired acoustic power levels that lead to a desired coating property. Similarly, the ANN model can be designed and trained to account for a single user input (for example a microhardness value) and multiple outputs (for example the SOD and PFR) to achieve the desired coating property as specified by the user.

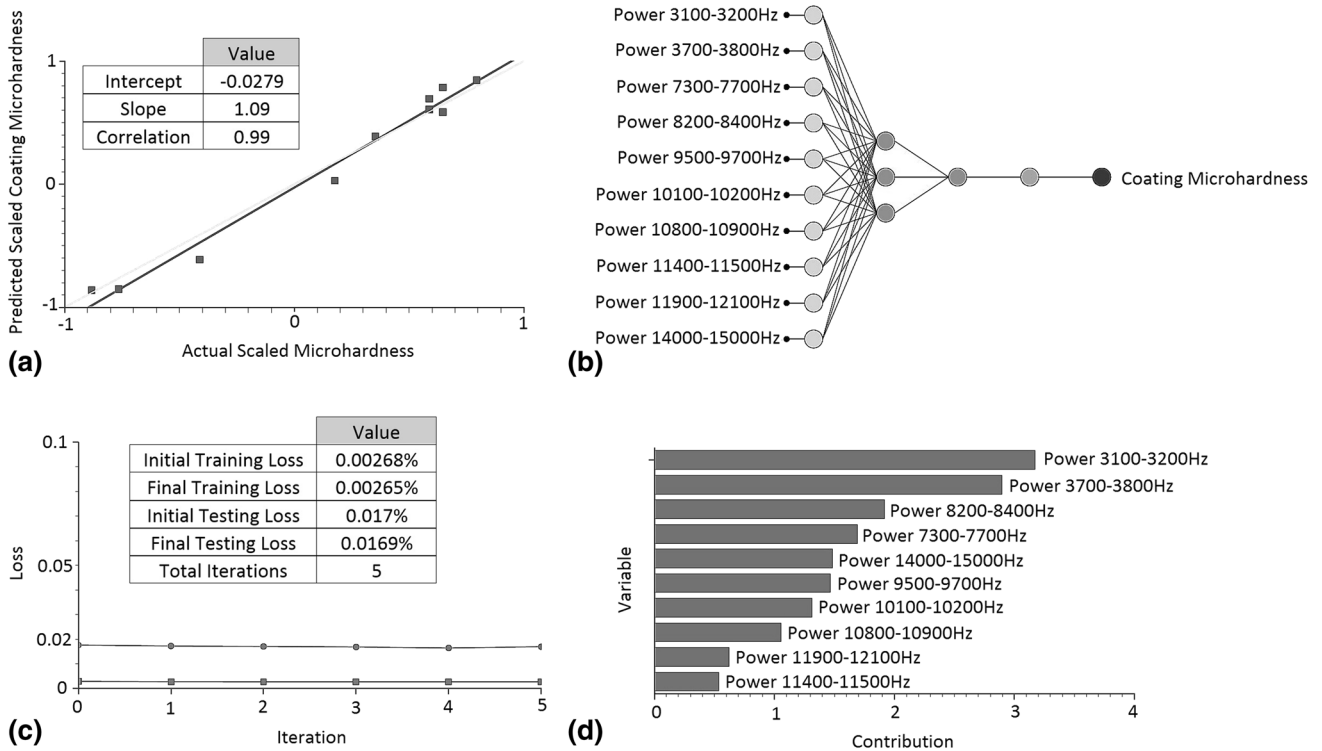


Fig. 13 (a) Linear regression analysis, (b) ANN architecture, (c) error calculations, (d) rating of input contribution to the outcome coating microhardness (HV0.3 kg)

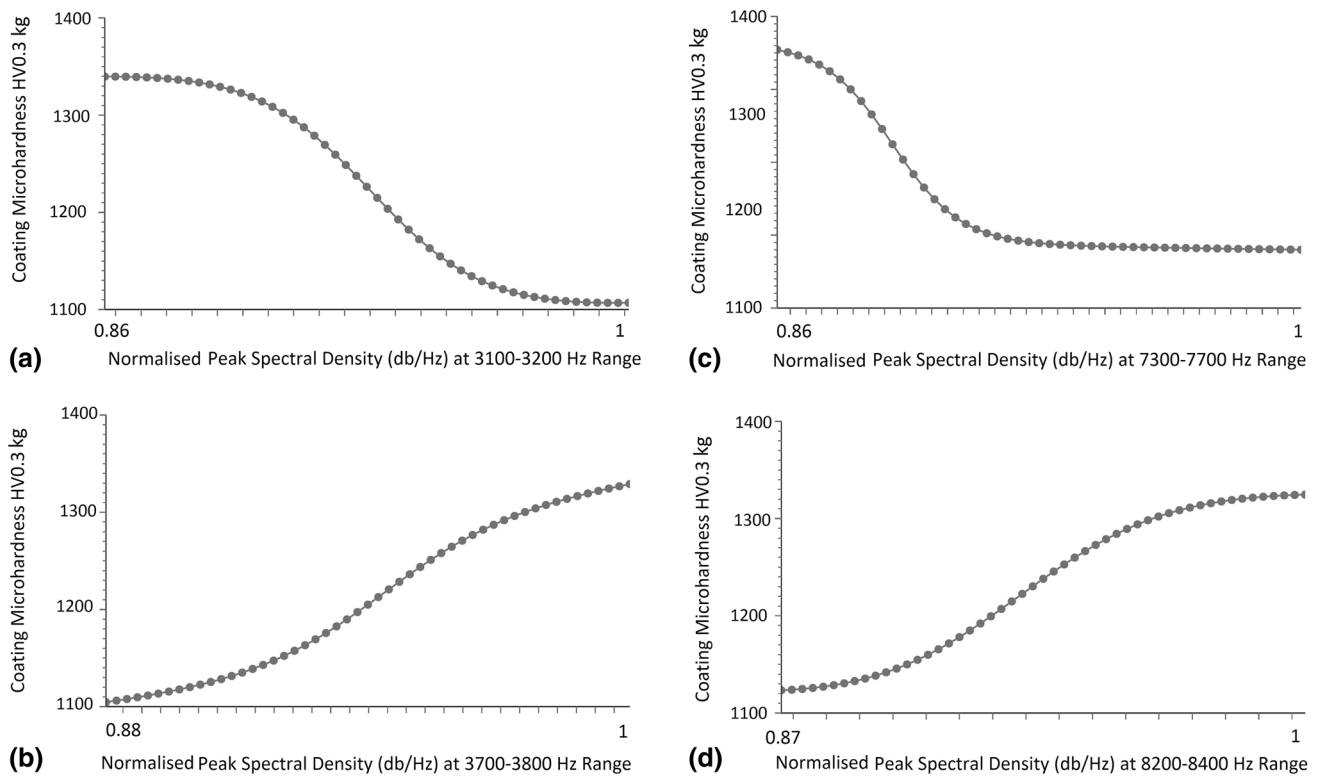
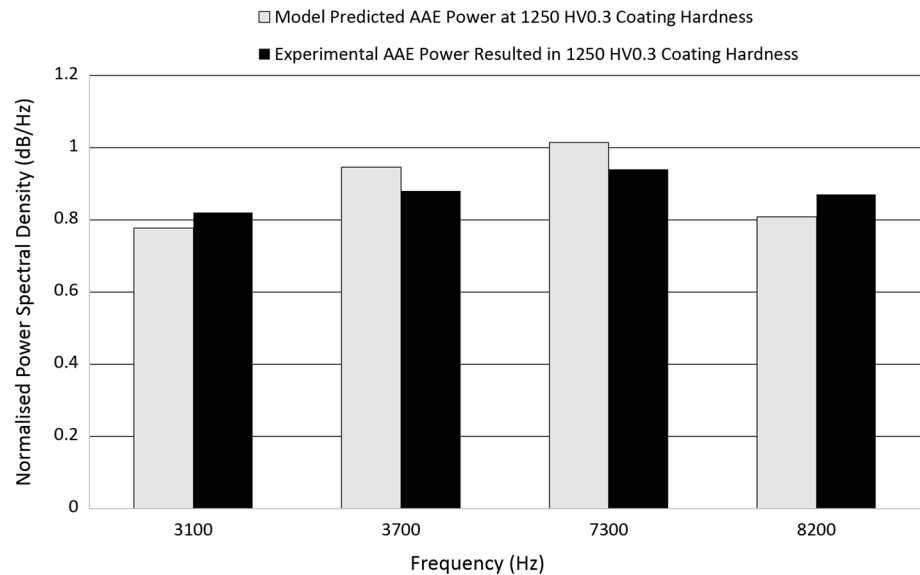


Fig. 14 Variation of coating microhardness (HV0.3 kg) as a function of a single power–frequency input. (a) Signal power at 3100-3200 Hz, (b) signal power at 3700-3800 Hz, (c) signal power at 7300-7700 Hz, (d) signal power at 8200-8400 Hz

Fig. 15 Unseen data predictive capability of the ANN. The spray distance was fixed at 120 mm, the powder feed rate was 2 kg/h, the traverse speed was 600 mm/s, and the impact angle was 90°



Conclusions

The main objective of the project was to demonstrate a methodology that could potentially lead to the design of a simple process monitoring device based on the airborne acoustic emissions generated during the HVOF or other high kinetic energy processes. The results demonstrate that intelligent sampling and QA monitoring linked to spray processing parameters is feasible. The work was executed in two main work packages. The first placed increased emphasis on the numerical modeling of the HVOF process aeroacoustics. The modeling data confirmed the presence of unique detectable noise features that can be attributed and correlated to several process variables, such as the powder feed rate and the standoff distance. Most importantly, this work demonstrated that the information carried in the raw acoustic dataset contains process variable-specific signatures that an ANN can benefit from producing meaningful outputs. The second work package focused on raw data analysis and classification by implementing several cost-effective shallow neural networks. Extensive error analysis and validation was carried out in order to finalize the model architecture. The ANN was trained using a relatively small experimental dataset; however, the input data were carefully selected and cleaned prior to ANN training. The generalization and predictive capability of the model has been successfully assessed and validated. The authors hope that this work will motivate more research on intelligent airborne noise sampling as an alternative method that can offer improved QA and QC to our thermal spray community.

Acknowledgments The authors would like to acknowledge the support from the UK Research & Innovation (UKRI) national funding agency. Project Grant: 132885.

References

- N.H. Faisal, R. Ahmed, R.L. Reuben, and B. Allcock, AE Monitoring and Analysis of HVOF Thermal Spraying Process, *J. Therm. Spray Technol.*, 2011, **20**(5), p 1071-1084
- H.A. Crostack, G. Reuss, T. Gath, and M. Dvorak, On-Line Quality Control in Thermal Spraying Using Acoustic Emission Analysis, Tagungsband Conference Proceedings, E. Lugscheider and R A. Kammer, Ed., March 17-19, 1999 (Düsseldorf, Germany), DVS Deutscher Verband für Schweißen, 1999, p 208-211
- E. Lugscheider, F. Ladru, H.A. Crostack, G. Reuss, and T. Haubold, On-line Process Monitoring During Spraying of TTBCs by Acoustic Emission Analyses, Tagungsband Conference Proceedings, E. Lugscheider and R A. Kammer, Ed., March 17-19, 1999 (Düsseldorf, Germany), DVS Deutscher Verband für Schweißen, 1999, p 312-317
- S. Nishinoiri, M. Enoki, and K. Tomita, In situ Monitoring of Microfracture During Plasma Spray Coating by Laser AE Technique, *Sci. Technol. Adv. Mater.*, 2003, **4**(1), p 623-631
- Y. Wang and P. Zhao, Noncontact Acoustic Analysis Monitoring of Plasma Arc Welding, *Int. J. Press. Vessels Pip.*, 2001, **78**(1), p 43-47
- W. Huang and R. Kovacevic, Feasibility Study of Using Acoustic Signals for Online Monitoring of the Depth of Weld in the Laser Welding of High-Strength Steels, *Proc. Inst. Mech. Eng. B J. Eng. Manuf.*, 2009, **223**(1), p 343-361
- E. Saad, H. Wang, and R. Kovacevic, Classification of Molten Pool Modes in Variable Polarity Plasma Arc Welding Based on Acoustic Signature, *J. Mater. Process. Technol.*, 2006, **174**(3), p 127-136
- L. Grad, J. Grum, I. Polajnar, and J. Marko Slabe, Feasibility Study of Acoustic Signals for On-line Monitoring in Short Circuit Gas Metal Arc Welding, *Int. J. Mach. Tools Manuf.*, 2004, **44**(5), p 555-561
- Y. Wang, Q. Chen, Z. Sun, and J. Sun, Relationship Between Sound Signal and Weld Pool Status in Plasma Arc Welding, *Trans. Nonferrous Metals Soc. Chin.*, 2001, **11**(1), p 54-57

10. W. Huang and R. Kovacevic, A Neural Network and Multiple Regression Method for the Characterization of the Depth of Weld Penetration in Laser Welding Based on Acoustic Signatures, *J. Intell. Manuf.*, 2011, **22**(2), p 131-143
11. S. Kamnis and S. Gu, Numerical Modelling of Propane Combustion in a High Velocity Oxygen-Fuel Thermal Spray Gun, *Chem. Eng. Process.*, 2006, **45**(4), p 246-253
12. S. Kamnis and S. Gu, 3-D Modelling of Kerosene-Fuelled HVOF Thermal Spray Gun, *Chem. Eng. Sci.*, 2006, **61**(16), p 5427-5439
13. ANSYS Fluent 19, Academic Edition, ANSYS, inc., 2018
14. J.E. Ffowcs-Williams and D.L. Hawkings, Sound Generation by Turbulence and Surfaces in Arbitrary Motion, *Proc. R. Soc. Lond.*, 1969, **264**(1), p 321-342
15. J. Smagorinsky, General Circulation Experiments with the Primitive Equations. I. The Basic Experiment, *Month. Weather Rev.*, 1963, **91**(1), p 99-164
16. B.F. Magnussen and B.H. Hjertager, On Mathematical Models of Turbulent Combustion With Special Emphasis on Soot Formation and Combustion, *Symp. (Int.) Combust.*, 1976, **16**(1), p 719-729
17. S. Kamnis, S. Gu, T.J. Lu, and C. Chen, Computational Simulation of Thermally Sprayed WC-Co Powder, *Comput. Mater. Sci.*, 2008, **43**(4), p 1172-1182
18. S. Gu and S. Kamnis, Numerical Modelling of In-Flight Particle Dynamics of Non-spherical Powder, *Surf. Coat. Technol.*, 2009, **203**(22), p 3485-3490
19. A.D. Gosman and E. Ioannides, Aspects of Computer Simulation of Liquid-Fuelled Combustors, *J. Energy*, 1983, **7**(6), p 482-490
20. "Neural Networks Tutorial 3. Neural network", Artificial Intelligence Techniques Ltd. (2019) www.neuraldesigner.com/learning/tutorials/neural-network. Accessed 12 Apr 2017
21. A. Pasini, Artificial Neural Networks for Small Dataset Analysis, *J. Thorac. Dis.*, 2015, **7**(5), p 953-960
22. K. Gurney, *An Introduction to Neural Networks, Master e-book ed, Chapter 11*, UCL Press Ltd., London, 2004
23. A. Krenker, M. Volk, U. Sedlar, J. Bešter, and A. Kos, Bidirectional Artificial Neural Networks for Mobile-Phone Fraud Detection, *ETRI, J.*, 2009, **31**(1), p 92-94
24. B. Kröse and P. Smagt, *An Introduction to Neural Networks, Chapter 4*, 8th ed., The University of Amsterdam, Amsterdam, 1996
25. R. Rojas, *Neural Networks: A Systematic Introduction, Chapter 7*, 1st ed., Springer, New York, 1996
26. J. Pulsford, S. Kamnis, J. Murray, M. Bai, and T. Hussain, Effect of Particle and Carbide Grain Sizes on a HVOAF WC-Co-Cr Coating for the Future Application on Internal Surfaces: Microstructure and Wear, *J. Therm. Spray Technol.*, 2018, **27**(5), p 207-219
27. V. Katranidis, S. Gu, B. Allcock, and S. Kamnis, Experimental Study of High Velocity Oxy-Fuel Sprayed WC-17Co Coatings Applied on Complex Geometries. Part A: Influence of Kinematic Spray Parameters on Thickness, Porosity, Residual Stresses and Microhardness, *Surf. Coat. Technol.*, 2017, **311**(1), p 206-215
28. V. Katranidis, S. Gu, T.R. Reina, E. Alpay, B. Allcock, and S. Kamnis, Experimental Study of High Velocity Oxy-Fuel Sprayed WC-17Co Coatings Applied on Complex Geometries. Part B: Influence of Kinematic Spray Parameters on Microstructure, Phase Composition and Decarburization of the Coatings, *Surf. Coat. Technol.*, 2017, **328**(1), p 499-512
29. "Diagnostic Electronics for Vibration Sensors VSE001", IFM Electronic Ltd. Kingsway Business Park, TW12 2HD, Great Britain, technical data (2007)
30. S. Kamnis, *Development of Multiphase and Multiscale Mathematical Models for Thermal Spray Process*, Aston University, Birmingham, 2008
31. C. Yu, W.R. Wolf, R. Bhaskaran, and S.K. Lele, Study of Noise Generated by a Tandem Cylinder Configuration Using LES and Fast Acoustic Analogy Formulations, AIAA Workshop in Aeroacoustics, 7-9 June 2010 (Stockholm, Sweden), AIAA (2010)
32. M. Wang and P. Moin, Dynamic Wall Modelling for Large-Eddy Simulation of Complex Turbulent Flows, *Phys. Fluids*, 2002, **14**(7), p 2043-2051
33. A.U. Zun, A.S. Lyrintzis, and G.A. Blaisdell, Coupling of Integral Acoustics Methods with LES for Jet Noise Prediction, *Int. J. Aeroacoust.*, 2005, **3**(4), p 297-346
34. D.W. Bechert and B. Stahl, Excitation of Instability Waves in Free Shear Layers Part 2. Experiments, *J. Fluid Mech.*, 1988, **186**(1), p 63-84
35. A. Pasini, V. Pelino, and S. Potestà, A Neural Network Model for Visibility Nowcasting From Surface Observations: Results and Sensitivity to Physical Input Variables, *J. Geophys. Res.*, 2001, **106**(14), p 951-959

Publisher's Note Springer Nature remains neutral with regard to jurisdictional claims in published maps and institutional affiliations.